RESEARCH ARTICLE

NANO · MICRO small
www.small-journal.com

Novel Structural Design and Adsorption/Insertion Coordinating Quasi-Metallic Na Storage Mechanism toward High-performance Hard Carbon Anode Derived from Carboxymethyl Cellulose

Yanhong Zhao, Zhuang Hu, Changling Fan, Peng Gao, Ruisheng Zhang, Zhixiao Liu, Jinshui Liu, and Jilei Liu**

Hard Carbon have become the most promising anode candidates for sodium-ion batteries, but the poor rate performance and cycle life remain key issues. In this work, N-doped hard carbon with abundant defects and expanded interlayer spacing is constructed by using carboxymethyl cellulose sodium as precursor with the assistance of graphitic carbon nitride. The formation of N-doped nanosheet structure is realized by the C–N• or C–C• radicals generated through the conversion of nitrile intermediates in the pyrolysis process. This greatly enhances the rate capability (192.8 mAh g^{-1} at 5.0 A g^{-1}) and ultra-long cycle stability (233.3 mAh g^{-1} after 2000 cycles at 0.5 A g^{-1}). In situ Raman spectroscopy, ex situ X-ray diffraction and X-ray photoelectron spectroscopy analysis in combination with comprehensive electrochemical characterizations, reveal that the interlayer insertion coordinated quasi-metallic sodium storage in the low potential plateau region and adsorption storage in the high potential sloping region. The first-principles density functional theory calculations further demonstrate strong coordination effect on nitrogen defect sites to capture sodium, especially with pyrrolic N, uncovering the formation mechanism of quasi-metallic bond in the sodium storage. This work provides new insights into the sodium storage mechanism of high-performance carbonaceous materials, and offers new opportunities for better design of hard carbon anode.

1. Introduction

In recent years, the large-scale application of lithium-ion batteries (LIBs) in electric vehicles, portable electronic devices, and smart grids, as well as the rapidly increasing cost of lithium resources, have become a challenge for the energy storage.[1–3] As a promising alternative, sodium-ion batteries (SIBs) have attracted extensive attention recently due to the abundant sodium resources and low cost. The practical application of SIBs depends on the development of electrode materials, especially the anode materials, which determines the performance of full batteries.[4–6] Unfortunately, the commercial graphite anode exhibits low capacity in SIBs due to its small interlayer spacing (0.3354 nm) and larger sodium ion radius (0.102 nm) than lithium ion radius (0.076 nm). Furthermore, the metal Na exhibits weaker binding to graphite anode compared with Li, meanwhile the formation energy of Na-graphite compounds is higher and more thermodynamically unstable.[7,8] Therefore, it is of great significance to find novel anode materials with low cost, rich resources, and excellent performance for SIBs.

In the past few decades, great progresses have been made to find suitable anode materials for SIBs, including carbonaceous materials (graphite,[9] graphene,[10] hard carbon[11]), metal/alloys (Sn,[12] Sb[13]), and metal oxide/sulfide (SnO_2,[14] TiO_2,[15] MoS_2,[16] SnS_2[17]). The carbonaceous materials are mostly intriguing because of their eco-friendliness, abundant resources, good chemical stability as well as low cost, which mainly consist of carbon spheres, carbon fibers, graphene, hard carbon, and so on.[18–23] Nevertheless, many carbonaceous materials exhibit

Y. Zhao, Z. Hu, C. Fan, P. Gao, R. Zhang, Z. Liu, J. Liu
College of Materials Science and Engineering
Hunan University
Changsha, Hunan 410082, P. R. China
E-mail: fancl@hnu.edu.cn; liujilei@hnu.edu.cn

The ORCID identification number(s) for the author(s) of this article can be found under https://doi.org/10.1002/smll.202303296

DOI: 10.1002/smll.202303296

C. Fan, J. Liu
Hunan Province Key Laboratory for Advanced Carbon Materials and Applied Technology
Hunan University
Changsha, Hunan 410082, P. R. China

C. Fan, P. Gao, J. Liu
Hunan Joint International Laboratory of Advanced Materials and Technology for Clean Energy
Hunan University
Changsha, Hunan 410082, P. R. China

poor rate capability, cycling performance, and low initial coulombic efficiency as the anode for SIBs. In order to improve the electrochemical performance of carbonaceous materials, it is considered as an efficient way to implement the heteroatomic doping strategy (e.g., B,[24] N,[25] P,[26] S[27]), which is believed can enhance the electrical conductivity, expand the carbon interlayer spacing, and increase the active sites of carbon materials, thus facilitating the rapid transportation of sodium ion and enhancing the sodium storage. Hao et al.[28] reported nitrogen doped porous carbon nanosheets derived from soft carbon for SIBs, which exhibited high capacity and electrical conductivity. Liu et al.[29] prepared nitrogen-doped graphene with superior rate capability, prominent ultra-long cycling life and much high coulombic efficiency up to 97.2%. Yang et al.[30] adopted N, S co-doping strategy to achieve the high-rate performance up to 110 mAh g^{-1} at 10 A g^{-1} for SIBs.

Hard carbon materials have a "house of cards" structure consisting of graphite-like microcrystals and amorphous region. The poor electrochemical performance can be improved by optimizing the morphology and structure of carbon materials. Lu et al.[31] synthesized 3D amorphous carbon with controlled porous and disordered structure, which delivered excellent rate performance and high reversible capacity up to 280 mAh g^{-1} at 30 mA g^{-1}. Xu et al.[32] prepared carbon microspheres with hierarchical architecture, which achieved high reversible capacity, excellent cycling stability and superior rate performance as high as 130 mAh g^{-1} at 10 A g^{-1}. Liu et al.[33] prepared carbon/graphene hybrid materials such as sandwich-like structures with graphene nanosheets coated on both sides of amorphous carbon layers, realizing high reversible sodium storage capacity of 336 mAh g^{-1} at 30 mA g^{-1}. Hong et al.[34] elaborately designed structure construction by tailoring carbon quantum dots for the first time, and obtained N-doped carbon with hollow nanostructures, which provided high reversible specific capacity.

Understanding the sodium storage mechanism of hard carbon materials is crucial to address the challenges faced by these materials. In 2000, Stevens et al.[35] prepared hard carbon materials through the pyrolysis of glucose and first proposed the "intercalation/adsorption" mechanism, which indicates that the sloping capacity is mainly derived from the intercalation of Na^+ into graphite-like layers, while the plateau capacity comes from the adsorption of Na^+ in the nanopores of the material. In 2012, Cao et al.[36] reported on a hollow carbon nanowire synthesized through direct pyrolysis of hollow polyaniline nanowire and proposed the "adsorption/intercalation" mechanism. This mechanism posits that the sloping capacity mainly comes from the adsorption of Na^+ on the carbon surface and edge defects, while the plateau capacity comes from the intercalation of Na^+ between graphitic carbon layers. Chen et al.[37] synthesized hard carbon materials by using glucose and magnesium gluconate as carbon sources to investigate the sodium storage mechanism. They monitored that the plateau capacity of hard carbon is contributed by both interlayer intercalation and micropore filling, therefore, they proposed a microstructure-dependent sodium storage mechanism, a hybrid "adsorption-intercalation/filling" mechanism.

However, ambiguous sodium storage mechanism of hard carbon anode materials hinders the rational design of their structure and the optimization of electrochemical performance. Huang et al.[38] found that hard carbon anode material delivers high reversible capacity and long-term cycling stability, attributing to the adsorption mechanism for sodium storage. Qiu et al.[39] revealed the adsorption/insertion mechanism of sodium storage in nonporous hard carbon by in situ X-ray diffraction mapping, ex situ nuclear magnetic resonance and electron paramagnetic resonance technologies, achieving high reversible capacity and coulombic efficiency. Bai et al.[40] described the design strategy for the relationship between high-performance and sodium storage mechanism by filling sulfur into microporous carbon, which confirmed the adsorption/filling mechanism of sodium ion in hard carbon.

Herein, we have systematically investigated the sodium storage mechanism of hard carbon and designed its structure rationally to realize superior electrochemical performance. As a typical easy-to-prepare cellulose derivative, CMC-Na has abundant hydrophilic functional groups on the surface, which can maintain strong interaction with the active load even after the carbonization. However, CMC-Na was found to be easily concentrated and agglomerated into blocks during the carbonization process, forming abundant disordered amorphous microstructure, which is unfavorable for sodium storage. In order to solve this issue, it is crucial to construct the amorphous carbon with appropriate ordered structure and suitable interlayer spacing. Therefore, in this work, N-doped carbon nanosheets (N-CNS) with optimized structure and morphology were prepared by the pyrolysis of common CMC-Na with the assistance of g-C_3N_4 via a freeze-drying technique. Carboxymethyl cellulose sodium (CMC-Na) was chosen as carbon source, given it is a derivative of cellulose with abundant, low-cost, and eco-friendly green renewable resources.[41–44] G-C_3N_4 exhibits rich nitrogen and unique 2D layered structure, which enables it to become an ideal self-sacrificing template for the synthesis of N-doped carbon materials.[45,46] The N-CNS displays high specific surface area, abundant active sites, and suitable interlayer spacing for sodium storage. Benefiting from the synergistic effects between layered structure and graphitized micromorphology, the N-CNS exhibits high reversible capacity, superior rate and cycling performance, which is promising for the practical application in SIBs as anode material.

2. Results and Discussion

2.1. Structure and Morphology

The carbon materials were synthesized by a facile one-step calcination of the as-prepared precursor CMC-Na@g-C_3N_4 under Ar atmosphere at various temperatures, denoted as N-CNS-T (T = 900, 1050, 1200). The schematic diagram of the formation of N-CNS is illustrated in **Figure 1**a. For comparison, the hard carbon derived from CMC-Na was prepared at 1050 °C, which is labeled as HC. The composite of CMC-Na@g-C_3N_4 is formed by the interaction of hydrogen bonding, as illustrated by FT-IR and XRD analysis in Figure S1 and S2, Supporting Information.

The crystal structures of N-CNS-T were analyzed by XRD, as shown in Figure 1b. HC shows the broad peak at around 23.0°, indicating a typical amorphous structure.[47] In comparison, N-CNS-T displays a similar broad peak at about 23.0° and another obvious peak near 43.8°, which are assigned to the (002) and (100)

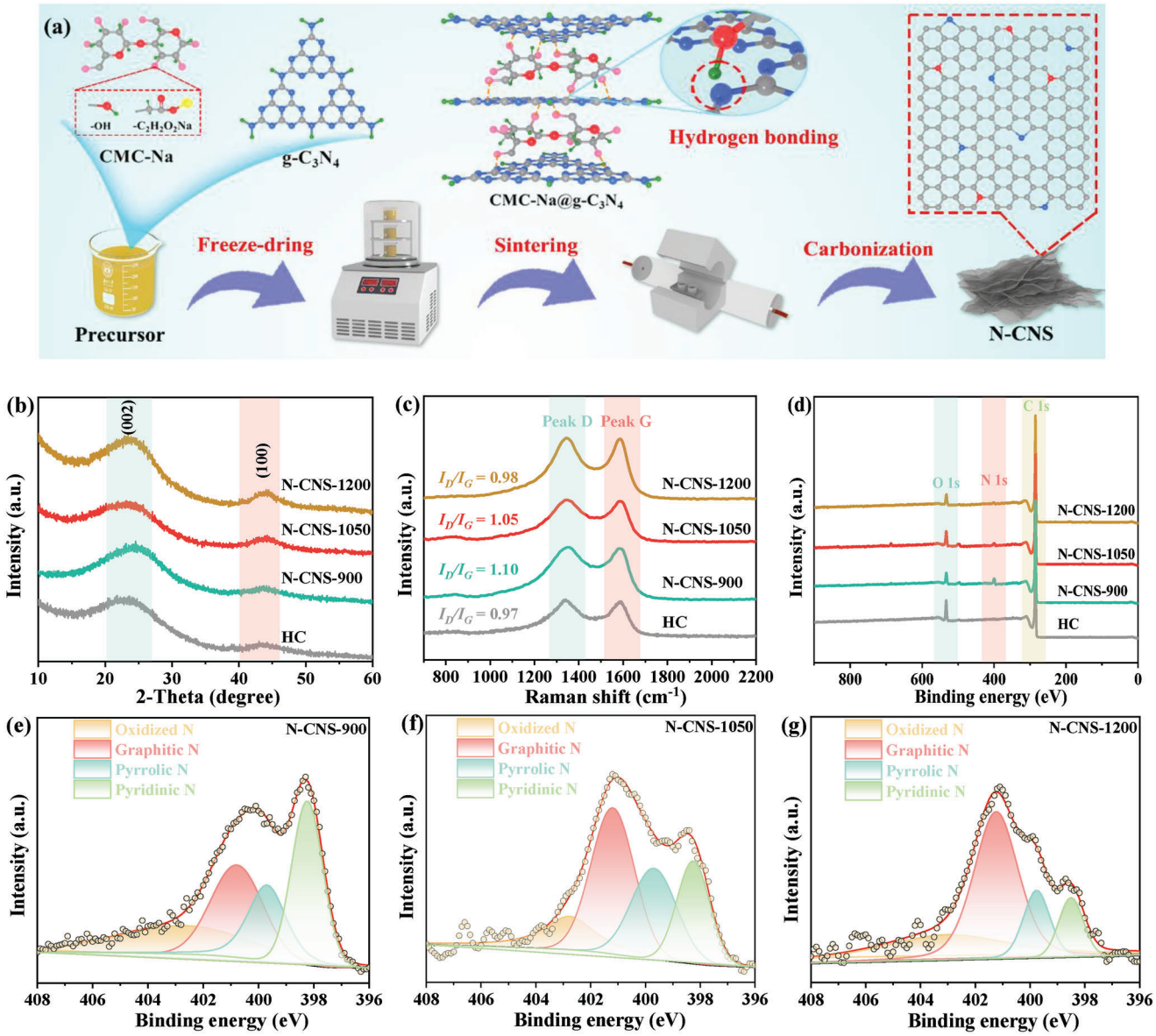

Figure 1. Schematic illustration of the formation of a) N-doped carbon nanosheets, b) XRD patterns, c) Raman spectra, d) XPS survey spectra, e–g) high-resolution N 1s spectra for HC, N-CNS-900, N-CNS-1050, and N-CNS-1200.

planes of graphite[48] and also demonstrating the characteristics of the amorphous structure.

Notably, N-CNS-1050 exhibits broad peak centered at about 22.9°, which is smaller than that of N-CNS-900 (24.4°) and N-CNS-1200 (23.6°). The negative shift of (002) peak reflects the expansion of interlayer spacing. The d_{002} is calculated according to the Bragg's diffraction Equation (1), where λ represents the wavelength of X-ray, θ is the half diffraction angle, d is the average interlayer spacing. The d_{002} values of stacked graphite sheets in N-CNS-900, N-CNS-1050, and N-CNS-1200 are calculated to be 0.364, 0.388, and 0.377 nm. The average lateral size (L_a) and stacking height (L_c) of graphite domain are calculated by the Scherrer Equation (2), as shown in Table S1, Supporting Information, where β is the full width at the half maximum intensity, and K is the shape factor of crystallite. It is believed that the increase of interlayer spacing and graphitic size are advantageous for the insertion/extraction of sodium ion.

$$2d \sin\theta = n\lambda \quad (1)$$

$$L = K\lambda/\beta \cos\theta \quad (2)$$

The Raman spectra of N-CNS-T were further obtained to evaluate the graphitization degree of carbon materials, as shown in Figure 1c. Two characteristic peaks (D band at ≈1345 cm^{-1} and G band at ≈1590 cm^{-1}) were obviously observed, corresponding to the defect-induced disordered structure and regular graphitic

carbon respectively. The intensity ratio of I_D/I_G is widely used to evaluate the degree of graphitization of carbon materials. N-CNS-900 exhibits higher I_D/I_G ratio of 1.10 compared to that of N-CNS-1050 (1.05) and N-CNS-1200 (0.98), suggesting the increased local ordering of graphitic carbon with the increase of calcination temperature.[49,50] The I_D/I_G ratios of N-CNS-T are higher than that of HC (0.97), presumably attributing to the increasing structural defects induced by N-doping.

The X-ray photoelectron spectroscopy (XPS) measurement was conducted to survey the elemental composition and chemical state of N-CNS-T, as shown in Figure 1d. There are three peaks in N-CNS-T assigning to C 1s (284.7 eV), N 1s (399.0 eV) and O 1s (531.2 eV), confirming the successful incorporation of nitrogen atoms. With the increase of temperature, the intensity of N 1s peak decreases and the content of N in N-CNS can be tuned gradually from 4.95 to 1.84 at%, displayed in Table S2, Supporting Information. In addition, all the high-resolution N 1s spectra of N-CNS-T can be deconvoluted into four peaks at 398.2, 399.7, 401.2, and 403.0 eV, attributing to the pyridinic N, pyrrolic N, graphitic N, and oxidized N, respectively, as shown in Figure 1e–g.[18] From Table S3, Supporting Information, it can be found that both the total N content and the configurations of N can be tuned through controlling the temperature. It is believed that the pyridinic N and pyrrolic N can provide active sites for sodium ion and contribute to the improvement of specific capacity, meanwhile the pyrrolic N with lone pair electron that is perpendicular to the graphene plane can significantly increase the interlayer spacing and reduce the energy barrier for sodium ion insertion.[45] Moreover, the graphitic nitrogen can bring extra free electrons to increase the electrical conductivity of graphene. Therefore, the appropriate doping content and configurations of N are essential to optimize the performance of N-CNS-T anode materials. The optimum configurations of N in N-CNS-1050 are expected to provide excellent electrochemical performance for SIBs.

The N_2 absorption/desorption isotherms were used to evaluate the Brunauer–Emmett–Teller (BET) specific surface area and pore structure of N-CNS-T. As displayed in Figure S3a, Supporting Information, all adsorption curves display the type I/IV shape with hysteresis loop, indicating the coexistence of micropores and mesopores.[51] However, there is a slight upward trend for HC at high relative pressure ($P/P_o = 0.96$–1.0), corresponding to the existence of macropores. Based on the BET analysis, the specific surface area of HC is calculated to be 748 $m^2\ g^{-1}$, which is larger than the N-CNS-T samples (491 $m^2\ g^{-1}$ for N-CNS-900, 396 $m^2\ g^{-1}$ for N-CNS-1050 and 341 $m^2\ g^{-1}$ for N-CNS-1200) as summarized in Table S4, Supporting Information. Moreover, the HC has a plenty of micropores with total volume of 0.46 $cm^3\ g^{-1}$ and the pore sizes are mainly centered at 0.5–0.7 nm (Figure S3b, Supporting Information). In contrast, the N-CNS-T samples present lower pore volumes of 0.23–0.27 $cm^3\ g^{-1}$ with micro- (<2 nm) and meso- (2–3 nm) pores. Specifically, the average pore sizes of HC and N-CNS-T are 2.16, 2.27, 2.74, and 2.61 nm, respectively. The optimized pore structure of N-CNS-1050 can facilitate the rapid transportation of electrons and ions, thus enhancing the electrical conductivity and improving the electrochemical performance of anode for SIBs.

The structures and morphologies of the as-obtained N-CNS-T were characterized by scanning electron microscopy (SEM) and high-resolution transmission electron microscopy (HRTEM). In **Figure 2**a, HC exhibits a micron-thick bulk structure formed by the agglomeration of irregular particles, constituting a hierarchical porous and highly disordered amorphous structure, which is further revealed by the HRTEM images, as shown in Figure 2b,c. However, the incorporation of g-C_3N_4 leads to a considerably different structure of as-synthesized N-CNS-T compared to HC (Figure 2d,g,j), which consisted of a layered nanosheet structure with rough and wrinkled surface, evidenced by the plenty of wrinkled graphene structure in the HRTEM images shown in Figure 2e,h,k. This structure is beneficial for increasing the contact surface between the electrode and electrolyte, allowing the sufficient penetration of electrolyte into the electrode and shortening the transportation distance of sodium ions. The HRTEM images in Figure 2f,i,l further reveal the microscopic morphology of N-CNS-T. With the increase of pyrolysis temperature, more graphene fragments, and clearer, regular lattice fringes of carbon layer have been observed. More importantly, the interplanar spacing of graphene layer in N-CNS is assessed by using the DigitalMicrograph software. The interlayer spacing of N-CNS-1050 is significantly expanded from 0.365 nm of N-CNS-900 to 0.388 nm, in good line with the XRD results, possibly attributing to the suitable doping content and configuration of N. Such increase in interlayer spacing will facilitate the insertion/extraction of sodium ions, accelerating the ions/electrons transportation. In addition, the increased rearrangement of graphene fragments leads to discontinuous lattices or dislocations, resulting in the structural defects of graphitic carbon materials that can provide abundant active sites for sodium ions storage. The typical elemental mappings of N-CNS-T in Figure S4, Supporting Information reveal the presence and homogeneous distribution of elements C, N, and O, confirming the doping of nitrogen.

2.2. Structural Evolution Mechanism

To further elucidate the structural evolution of N-CNS-T, the precursor CMC-Na@g-C_3N_4 was characterized by in situ thermogravimetric analysis coupled to mass spectrometry (TG-MS) under Ar atmosphere. **Figure 3**a shows the TG and differential scanning calorimetry (DSC) curves of precursor CMC-Na@g-C_3N_4.

The 3D TG-MS curves of evolved gas in the annealing progress are displayed in Figure 3b and Figure S5, Supporting Information. There is a slight weight loss at about 110 °C, which is mainly due to the release of small molecules such as H_2O, CH_4 and NH_3. An exothermic peak at around 295 °C can be clearly observed, attributing to the decomposition reaction of cellulose including decarboxylation, dehydration, and molecular rearrangement, accompanied by the release of gases such as H_2O, CH_4, NH_3, CO, CO_2, and the formation of carbonaceous material.[42] A significant endothermic peak appears at 680 °C, which is related to the decomposition of g-C_3N_4 and releasing nitrogen-containing gas substances of N_2 and C_2N_2 (Figure 3c) for further doping reaction.[52] The weight loss was continued upon increasing the temperature, which is mainly associated with the rapid volatilization and oxidation of derived carbon, essentially the elimination of heteroatoms (O, N, H) from the carbonaceous material to increase the degree of graphitization.[53]

The FT-IR spectra of precursor CMC-Na@g-C_3N_4 sintered at various temperatures are shown in Figure 3d. According to the

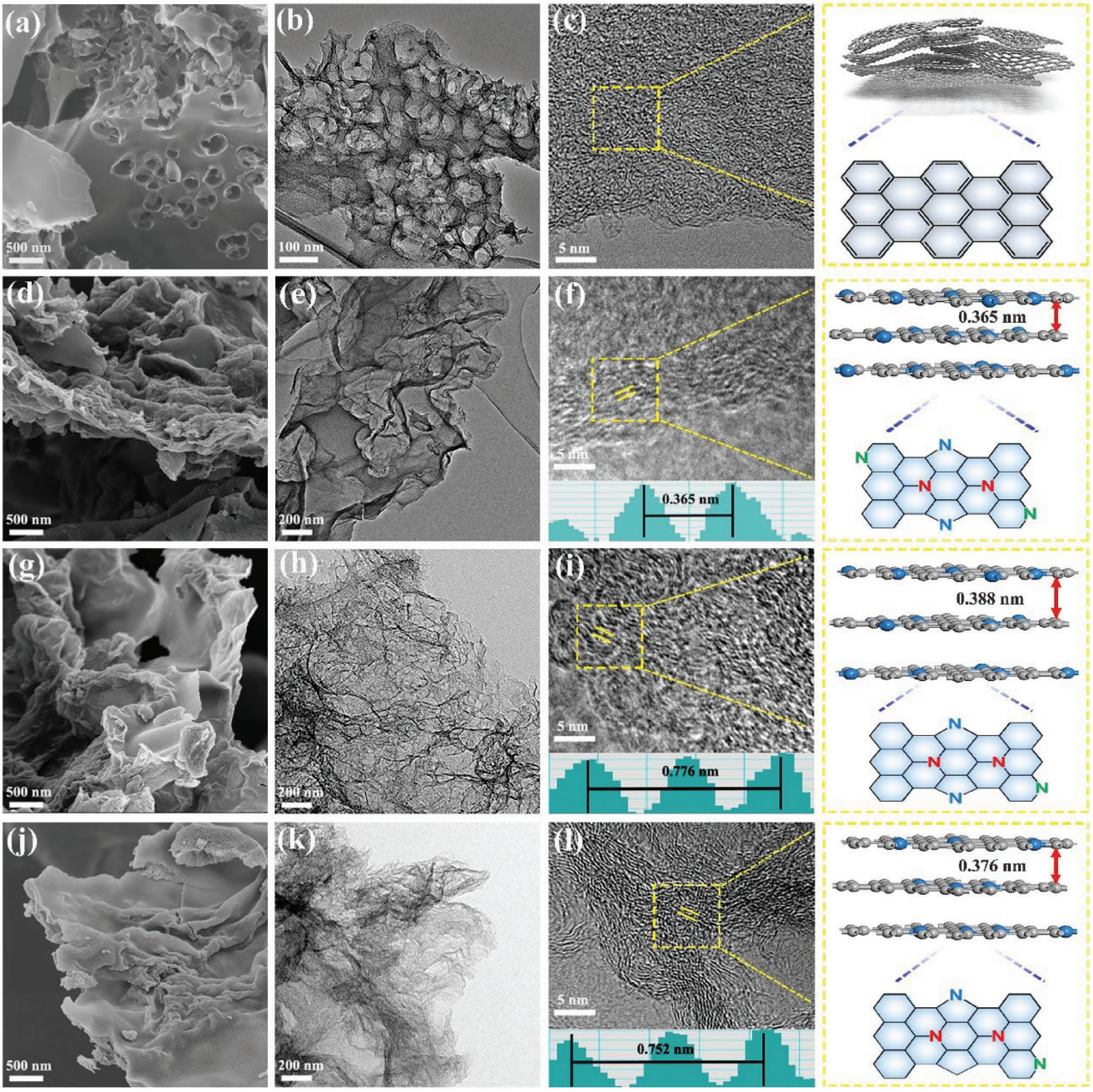

Figure 2. a,d,g,j) SEM images, b,c,e,f,h,i,k,l) HRTEM images (the intensity line profiles to the graphene layers in inset) for HC, N-CNS-900, N-CNS-1050, and N-CNS-1200.

typical FT-IR spectra of g-C_3N_4 (Figure S1, Supporting Information), the sample obtained by calcining the precursor at the temperature of 300 °C shows similar characteristic with that of g-C_3N_4, possibly due to the decomposition of CMC-Na and the disappearance of hydrogen bonding. When the temperature was increased from 300 to 600 °C, g-C_3N_4 is gradually decomposed, accompanied with the formation of nitrile intermediates.[46] After heating to 700 °C, the C=N bond (≈1600 cm^{-1}) and C–N bond (≈1360 cm^{-1}) are formed obviously, indicating the successful formation of N-doped carbon material.[54,55] When the temperature is further increased, the vibrational intensities of these groups weaken gradually, attributing to the gradual decrease of nitrogen-containing bonds. The appropriate doping of N can not only improve the electrical conductivity of material, but also provide more active sites for sodium-ion storage. However, the excessive doping of nitrogen is not conducive to the formation of local graphitization structure, which will reduce the electrical conductivity. Similarly, the low N doping content leads to fewer active sites, thus decreasing the sodium ions storage capacity.

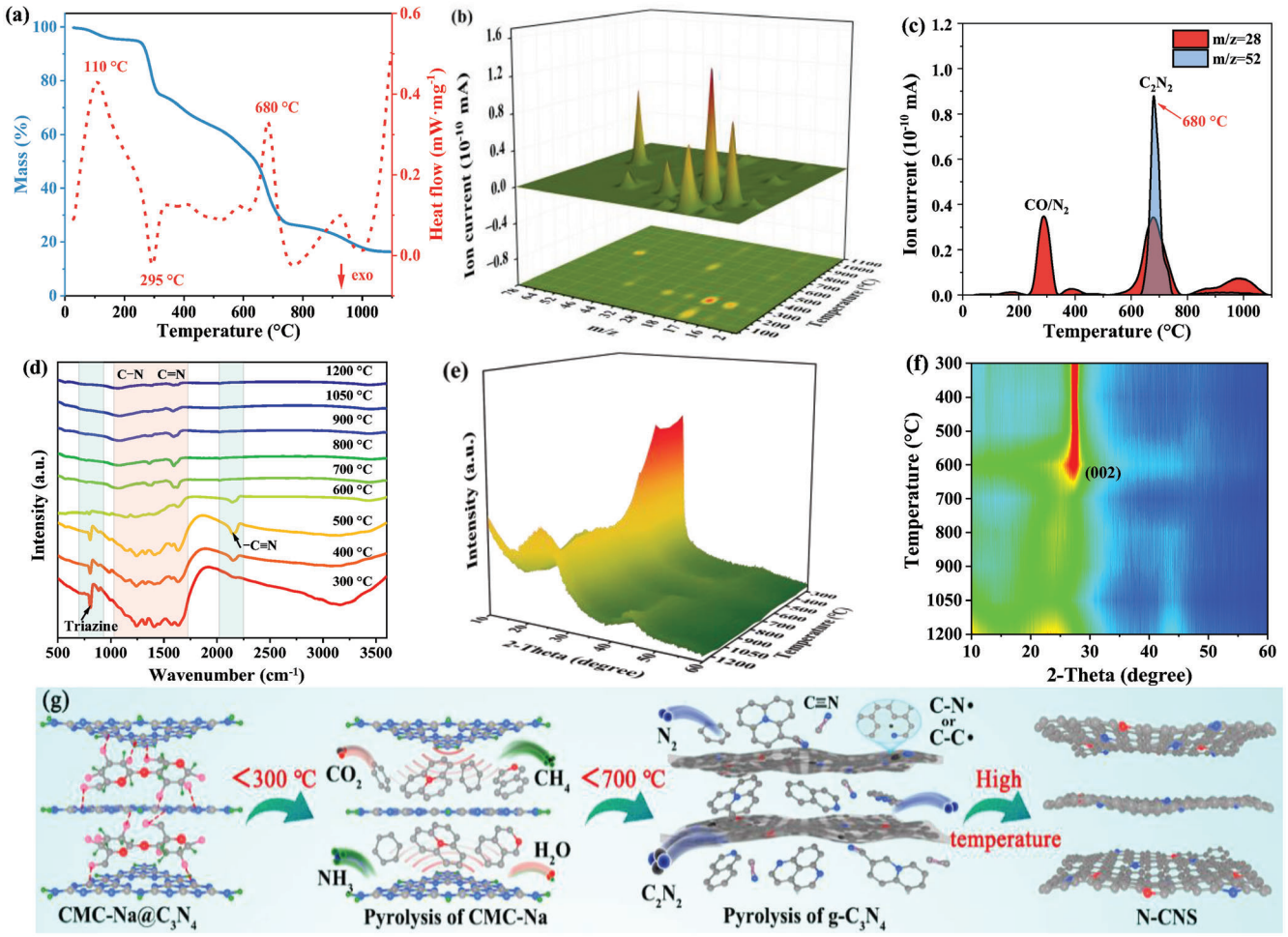

Figure 3. Structural evolution of a) TG/DSC curves, b) 3D TG-MS curves, c) signal strength of CO/N_2 (m/z = 28) and C_2N_2 (m/z = 52), d) FT-IR spectra, e) 3D XRD patterns, f) XRD contour plot of precursor CMC-Na@g-C_3N_4 at different annealing temperatures under Ar atmosphere, g) construction mechanism of N-CNS.

The transformation of precursor was further confirmed by the XRD patterns obtained at various temperatures, as shown in Figure 3e,f and Figure S6, Supporting Information. At 300 °C, the characteristic diffraction peak of CMC-Na is not observed (typically at about 20.1°), whereas only the characteristic peaks of g-C_3N_4 are presented, indicating that the CMC-Na is decomposed at this stage. As the temperature increases from 300 to 600 °C, the (100) peak at 13.0° gradually disappears and the (002) peak at 27.3° also decreases significantly. At the temperature of 700 °C, a new broad (002) peak at 25.2° is emerged, which is belonging to the carbon material and suggesting that the g-C_3N_4 is completely decomposed and the amorphous carbon is successfully formed, consistent with the TG and FT-IR analysis. When the temperature increased progressively, the structure of as-prepared carbon is further optimized by adjusting the nitrogen content and graphitization degree. Until 1050 °C, the (002) peak of the obtained carbon shifts to the lowest diffraction angle, delivering the largest interlayer spacing, which is attributed to the optimized nitrogen configuration and graphitic carbon.

Based on the above analysis, we propose a possible mechanism for the construction of N-doped carbon nanosheets, schematically illustrated in Figure 3g. CMC-Na has large number of hydroxyl groups, which can be strongly bound to the g-C_3N_4 template by hydrogen bonding. During the low temperature pyrolysis, g-C_3N_4 with layered structure can provide favorable structural skeleton for the formation of 2D carbon nanosheet during the thermal condensation reaction of CMC-Na. In the process of thermal polymerization, the N-doped carbon is formed through the conversion of nitrile intermediates, in which C–N• or C–C• radicals are generated and defect-rich carbon skeletons are formed. When the temperature is increased to over 700 °C, the g-C_3N_4 template is completely decomposed and the N-doped carbon material is successfully formed. With the further increment of temperature, the doping content and nitrogen configuration in carbon materials are adjusted, and the local graphitization region in amorphous carbon is realized, thus resulting in the synthesized graphene carbon nanosheets with suitable layer spacing for the sodium storage and high electrical conductivity.

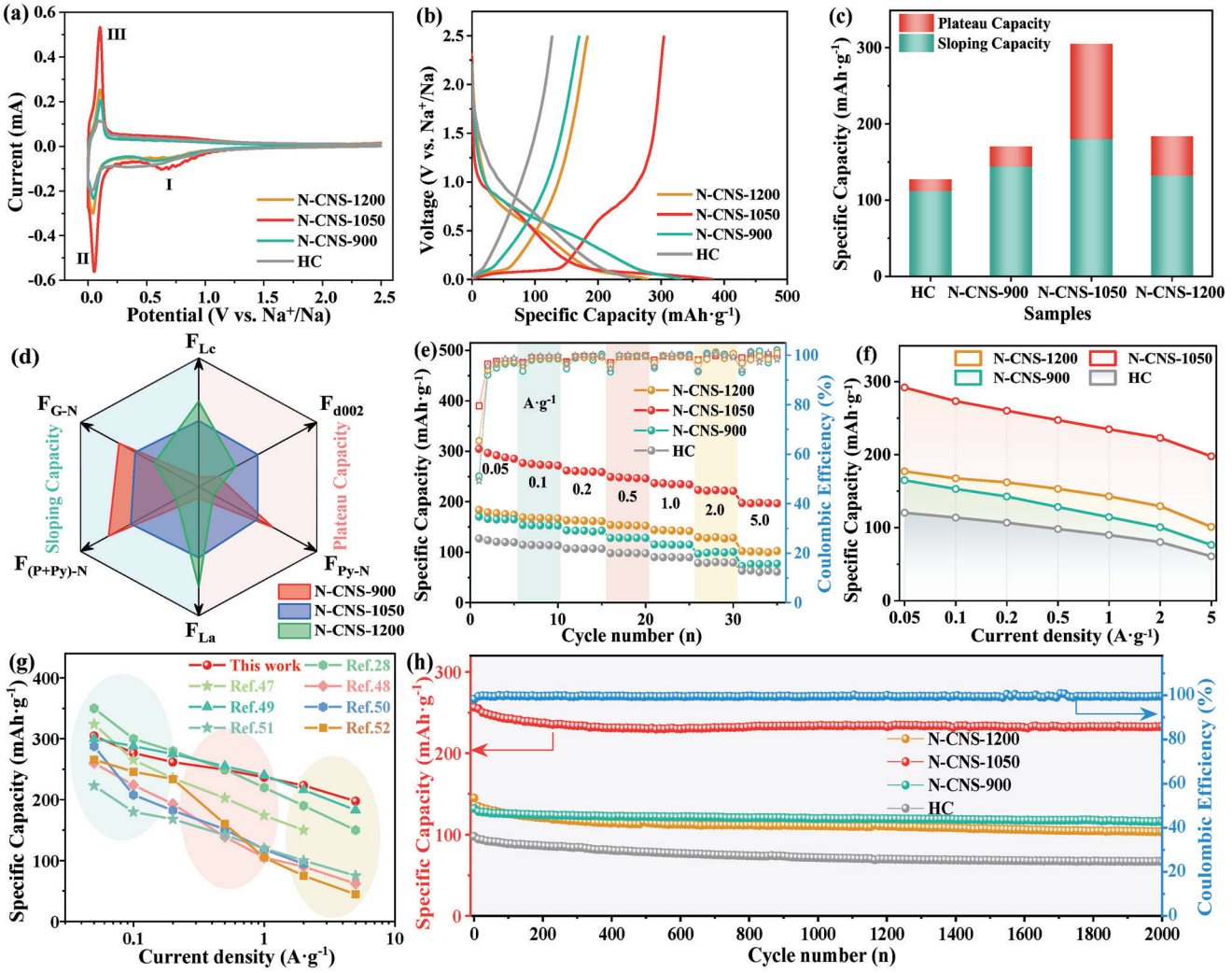

Figure 4. a) CV curves of N-CNS anodes in the first cycle, b) galvanostatic discharge/charge profiles in the initial cycle at 0.05 A g^{-1}, c) the plateau and sloping capacity distribution below and above 0.1 V, d) the influence factors of plateau and sloping capacity and contributions to capacity (G-N, P-N, and Py-N are graphitic N, pyridinic N, and pyrrolic N, respectively), e,f) rate performance and the corresponding coulombic efficiency of N-CNS anodes, g) comparison of rate performance for N-CNS-1050 in this work with carbon anodes reported in some literatures, h) long-term cycling performance at 0.5 A g^{-1} for HC, N-CNS-900, N-CNS-1050, and N-CNS-1200.

2.3. Electrochemical Performance

To investigate the electrochemical performance of N-CNS-T anodes, cyclic voltammetry (CV), galvanostatic discharge/charge, rate capability, and cycling stability tests were performed. **Figure 4**a presents CV curves of the first cycle for N-CNS-T and HC anode at a scan rate of 0.1 mV s^{-1} between 0.0 and 2.5 V (vs. Na^+/Na). A broad cathodic peak I at about 0.35–0.68 V is obviously observed in the first cycle, attributing to the decomposition of electrolyte and the formation of solid electrolyte interface (SEI) film on the electrode surface.[56] A pair of sharp redox peaks II/III appear at around 0.0–0.1 V during the cathodic/anodic scanning processes, indicating the reversible insertion/extraction of sodium ions between graphite layers. A pair of weak and broad humps are also observed in the voltage region of 0.1–1.5 V, corresponding to the adsorption of sodium ions on the defect sites and edges of graphitic domains. However, the integrated area of irreversible peak I of HC is larger than that of N-CNS-T, indicating that more severe irreversible reactions are occurred on the electrode surface, with a lower initial coulombic efficiency. In Figure S7, Supporting Information, the CV curves of N-CNS are almost overlapped after the first cycle, indicating superior reversibility for the insertion/extraction of sodium ions. In Figure S8, Supporting Information, the uneven deposition of electrolyte on the surface of HC anode after cycling can be observed from the optical micrographs. In contrast, the surface of N-CNS-1050 anode after cycling is smooth and uniform, which further supports the CV analysis.

The galvanostatic discharge/charge curves of N-CNS-T anodes at the current density of 0.05 A g^{-1} are shown in Figure 4b and Figure S7, Supporting Information. It can be observed that the curves contain two different voltage regions, a sloping region above 0.1 V and a low potential plateaus region below 0.1 V, attributing to the adsorption/desorption on the defect sites and

the insertion/extraction between the graphite layers of sodium ion, consistent with the CV analysis. N-CNS-1050 shows an initial reversible capacity of 304.7 mAh g^{-1}, which is much higher than that of 170.5 mAh g^{-1} for N-CNS-900, 183.6 mAh g^{-1} for N-CNS-1200, and 127.1 mAh g^{-1} for HC. The initial coulombic efficiencies of HC and N-CNS-900 (49.28%, 51.16%) are lower than that of N-CNS-1050 and N-CNS-1200 (79.52%, 65.40%), indicating that the irreversible reaction is more serious in the first cycle, which is consistent with the CV analysis.

In Figure S9, Supporting Information, it can be observed that the surface of HC anode is rough after three cycles, indicating that the electrolyte decomposes severely on the electrode. In contrast, the structure of N-CNS-1050 remains intact after the circulation, suggesting good compatibility between the electrode and electrolyte. Notably, in Figure 4c, N-CNS-T samples exhibit higher capacity in both regions than HC, and N-CNS-1050 anode exhibits the optimum plateau capacity and sloping capacity. Considering the effect of structure on electrochemical performance, our study showed that the plateau capacity is mainly affected by the formation of graphite domain size, carbon interlayer spacing and the content of pyrrolic nitrogen together, while the sloping capacity is mainly affected by the graphite domain area, nitrogen doping content and configurations, as shown in Figure 4d. Under the temperature-controlled adjustment of nitrogen doping, the influence factors of N-CNS-1050 reach a balanced proportional relationship, showing the best sodium storage capacity. In contrast, at the low temperature, N-CNS-900 exhibits a lower plateau capacity because of the smaller size of graphite microcrystal, resulting in less intercalated sodium despite high nitrogen doping content. When the temperature rises to 1200 °C, although the graphite domain increases, the interlayer spacing and nitrogen doping content decrease gradually, leading to the unsatisfactory capacity for N-CNS-1200 anode. Therefore, it can be concluded that optimizing the nitrogen doping content and configuration, enlarged interlayer spacing and locally increased graphite domains are beneficial to improve the overall electrochemical performance.

In order to further understand the electrochemical performance, Figure 4e,f displays the rate capacities of N-CNS-T anodes. The superior rate performance of N-CNS-1050 anode is extremely impressive. Specifically, N-CNS-1050 anode delivers the reversible capacities of 304.7, 276.7, 261.8, 249.2, 236.8, and 223.4 mAh g^{-1} at the current densities of 0.05, 0.1, 0.2, 0.5, 1.0, and 2.0 A g^{-1}, respectively. Even when the current density rises to 5.0 A g^{-1} (i.e., 16 C, 1 C = 300 mA g^{-1}), the capacity is as high as 197.6 mAh g^{-1}, which is superior to those reported carbon anode materials, as compared in Figure 4g.[30,57–62] The discharge/charge curves of N-CNS-T and HC at each current density are described in Figure S10a–d, Supporting Information. As compared with counterparts, it can be found that N-CNS-1050 exhibits smaller electrochemical polarization with increasing current density, attributing to the enlarged interlayer spacing and increased local graphitization. In Figure S11a,b, Supporting Information, the plateau capacity of the insertion between graphite layer for N-CNS-1050 anode increases slightly after the activation with small current, ascribing to the sufficient penetration of electrolyte into the electrode. With the increasing of current density, both the plateau capacity and the sloping capacity decrease because of the electrochemical polarization. In Figure S11b, Supporting Information, when the current density exceeds 1.0 A g^{-1}, the plateau capacity ratio decreases rapidly from 47.0% at 1.0 A g^{-1} to 27.4% at 5.0 A g^{-1}. Meanwhile, the corresponding sloping capacity ratio increases from 53.0% at 1.0 A g^{-1} to 72.6% at 5.0 A g^{-1}, illustrating that the kinetics of the sloping region associated with the defect adsorption is much faster than that of the plateau region related to the insertion of graphite layer. Figure 4h presents the long-term cycling performance of N-CNS-T anodes at the current density of 0.5 A g^{-1}. Compared with other samples, N-CNS-1050 anode delivers the highest reversible capacity and the best cycling stability. After 2000 discharge/charge cycles, N-CNS-1050 still delivers reversible capacity of 233.3 mAh g^{-1} and excellent capacity retention ratio of 90.9%. However, the reversible capacity of HC shows an obvious trend of decay, from 97.7 to 66.7 mAh g^{-1} with poor capacity retention ratio of 68.3% after 2000 cycles, probably due to its fewer defects and the instability of amorphous structure.

In general, N-CNS-1050 exhibits the best electrochemical performance, including considerably high capacity, excellent cycle stability, and superior rate capacity. This can be attributed to the following points. First, at a certain temperature, N-CNS-1050 possesses more graphitic carbon and expanded interlayer spacing up to 0.388 nm, which facilitates the insertion/extraction of sodium ion between carbon layer and buffers the volume expansion during the discharge/charge process. Second, the appropriate doping content and nitrogen configurations not only provide more active sites for sodium storage, but also improve the electrical conductivity of carbon materials. Third, the 2D carbon nanosheet structure can ensure sufficient contact between the electrode and electrolyte, shortening the transportation path of sodium ions and facilitating the rapid transportation of ions.

2.4. Sodium Ion Storage Mechanism and DFT Calculations

In order to better understand the relationship between the excellent electrochemical performance of N-CNS-1050 and its microstructure, the CV curves of hard carbon anode at different scan rates were obtained to further investigate the reaction kinetics and the mechanism of sodium ion storage. As displayed in **Figure 5**a,b, the redox peak current of anode gradually increases obviously with the increase of scan rate, delivering a functional relationship of Equation (3).[63] Where a and b are constants, b value can be obtained from the slope of the linear plot of $\ln(i)$–$\ln(v)$.

$$i = av^b \tag{3}$$

Particularly, $b = 1$ represents the surface-controlled capacitive process such as adsorption, and $b = 0.5$ represents the diffusion-controlled embedding process such as intercalation. By calculation, the b values of the cathodic and anodic peaks for N-CNS-1050 are 0.84 and 0.74, indicating that the capacitive process is dominant, and the diffusion process also exists in the sodium ion storage process. Likewise, other samples exhibit similar storage mechanism, as shown in Figure S12, Supporting Information. In addition, at a certain scan rate, the exact contribution proportion between these two electrochemical processes can be calculated

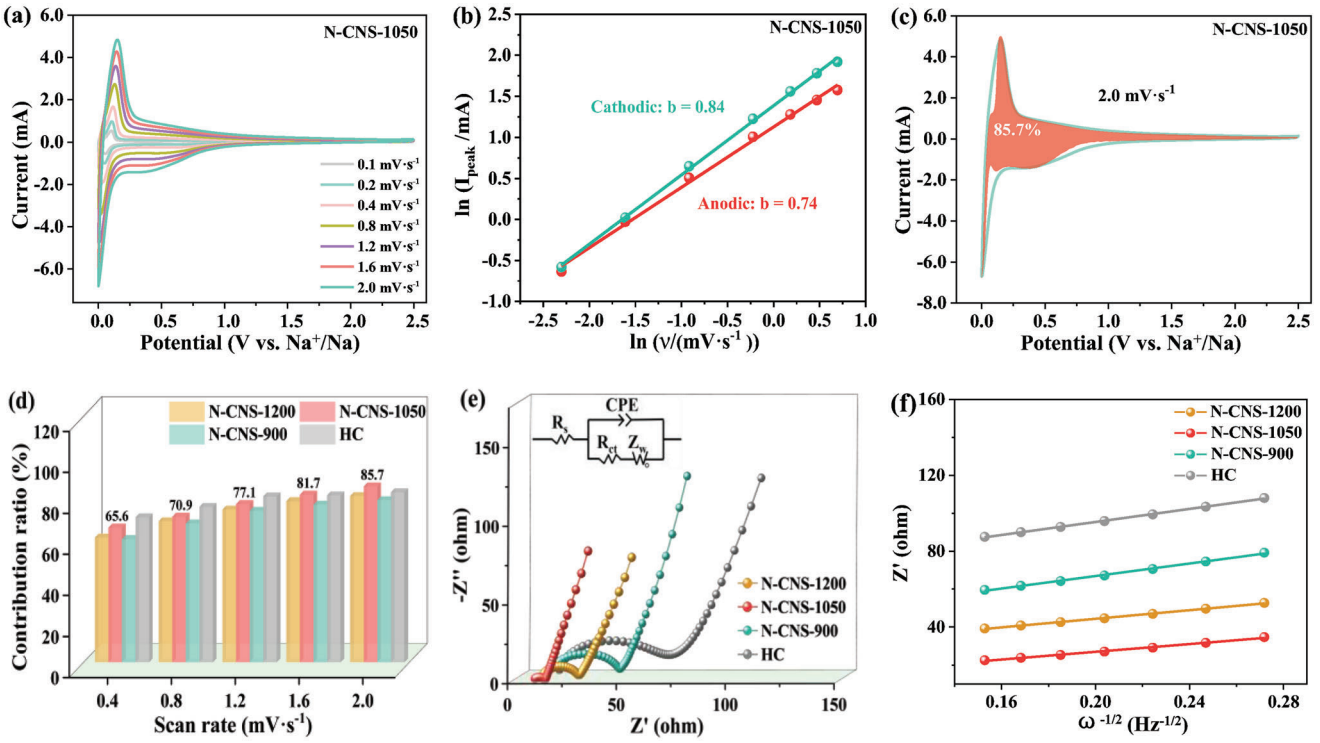

Figure 5. a) CV curves at various scan rates from 0.1 to 2.0 mV s^{-1} and b) the corresponding linearity relationship between ln(*i*) and ln(*v*) of cathodic and anodic peaks, c) capacitive contribution at a scan rate of 2.0 mV s^{-1} for N-CNS-1050, d) the contribution ratios of capacitive capacity at different scan rates, e) Nyquist plots and f) Z'–$\omega^{-1/2}$ plots for HC, N-CNS-900, N-CNS-1050, and N-CNS-1200.

by Equation (4).[64]

$$i = k_1 v + k_2 v^{\frac{1}{2}} \quad (4)$$

where $k_1 v$ and $k_2 v^{1/2}$ represent the contribution of surface capacitive and diffusion control process, respectively.

In Figure 5c, the capacitive contribution of N-CNS-1050 can reach a high value of 85.7% at the scan rate of 2.0 mV s^{-1}. The capacitive contribution ratios to the total capacity for samples at different scan rates are shown in Figure 5d. Compared with other samples, the capacitive contribution ratio of N-CNS-1050 are relatively high, attributing to its abundant active sites. The increased graphite domains with enlarged interlayer spacing also enhance the utilization of carbon layer at high current densities, thereby improving sodium storage capacity and electrochemical performance. However, the low capacity of HC is also resulted from capacitive contribution (82.8% at 2.0 mV s^{-1}), which may be related to the low degree of graphitization and highly disordered structure.

Electrochemical impedance spectroscopy (EIS) was performed to further analyze the diffusion characteristic of sodium ion in N-CNS-1050 anode. As shown in Figure 5e, all Nyquist plots are composed of a semicircle in high-frequency region related to charge transfer resistance (R_{ct}) and a sloping line in low-frequency region associated to the Warburg impedance (Z_w). The intercept of semicircle on the real axis in high-frequency region represents the resistance of electrolyte, the electrode and other intrinsic resistance (R_s). According to the corresponding equivalent circuit model in the inset in Figure 5e, the fitting results are listed in Table S5, Supporting Information. Obviously, the R_{ct} for N-CNS-1050 (5.3 Ω) is much smaller than that of N-CNS-900 (32.6 Ω), N-CNS-1200 (18.5 Ω), and HC (46.6 Ω), indicating that the intrinsic defects and expanded interlayer spacing are favorable to the charge transfer. In addition, the diffusion coefficient of sodium ion can be calculated by Equation (5),

$$D = R^2 T^2 / 2A^2 n^4 F^4 C^2 \sigma^2 \quad (5)$$

where *R*, *T*, and *A* denote gas constant, absolute temperature, and the surface area of the electrode. *n* and *F* represent the transfer number of electrons per molecule and Faraday constant. *C* is the molar concentration of sodium ion. σ is the slope of Z'–$\omega^{-1/2}$ plots. By fitting the plot of Z' and $\omega^{-1/2}$, as shown in Figure 5f, the diffusion coefficient of N-CNS-1050 is calculated to be 1.4×10^{-12} cm^2 s^{-1}, which is much higher than that of N-CNS-900 (5.5×10^{-13} cm^2 s^{-1}), N-CNS-1200 (1.2×10^{-12} cm^2 s^{-1}), and HC (5.1×10^{-13} cm^2 s^{-1}) in Table S5, Supporting Information. The results further demonstrate that superior diffusion property can enhance the rate capability of N-CNS-1050 as SIB anode. Compared with reported related carbon materials in Table S6, Supporting Information, N-CNS-1050 exhibits better electrochemical performance in sodium ion batteries.

To further investigate the sodium ion storage mechanism, the structural evolution of N-CNS-1050 during the discharge/charge process was characterized by in situ Raman, ex situ XRD, and XPS. For HC anode, as shown in **Figure 6**a–c, neither significant reduction in intensity of the *G*-band nor corresponding plateau region appears, meanwhile the discharge curve displays smooth

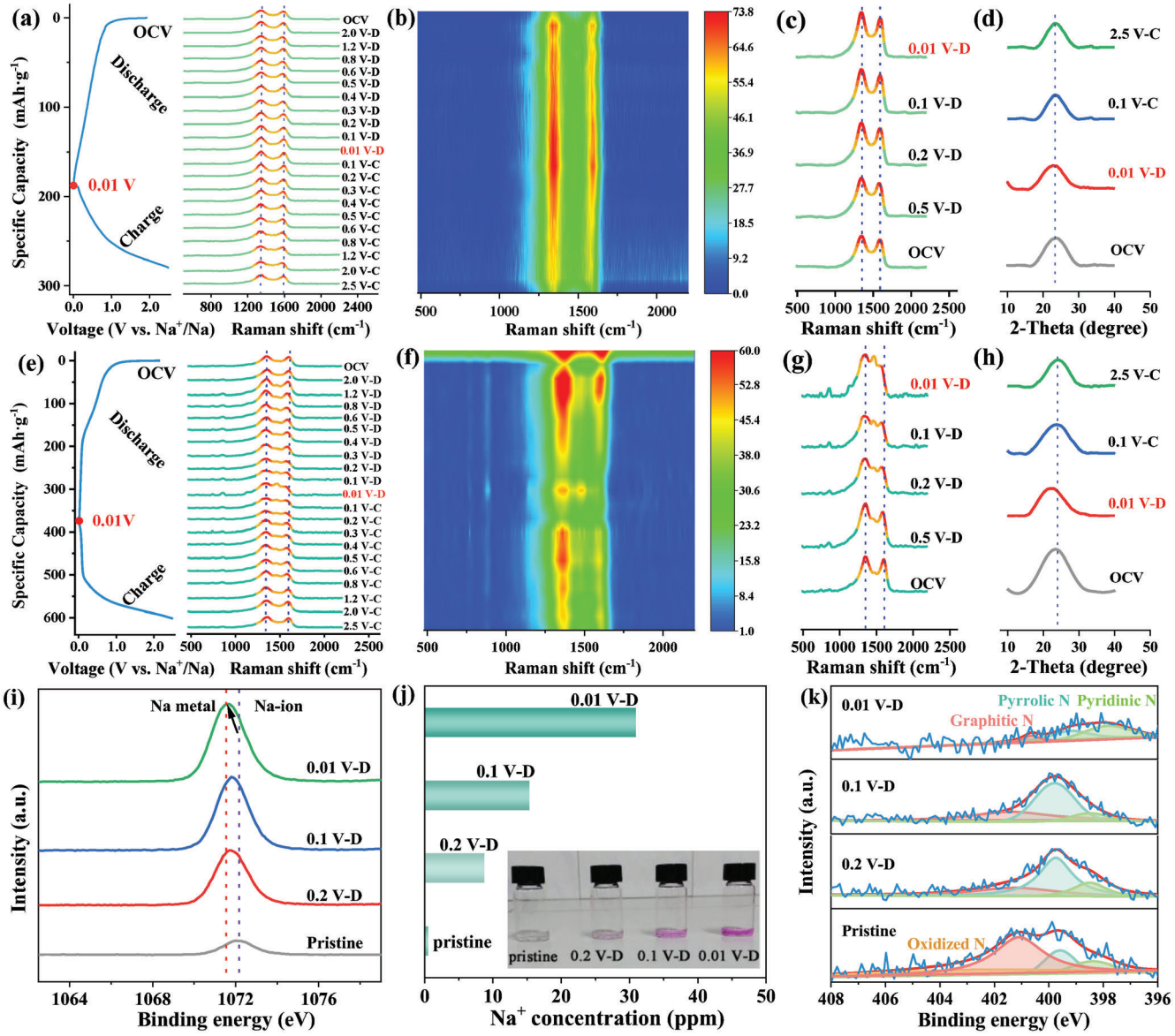

Figure 6. a–c) In situ Raman spectra of HC and e–g) N-CNS-1050, d) ex situ XRD patterns at different stages of HC and h) N-CNS-1050 in the first cycle, i) ex situ XPS Na 1s spectra, the concentration of Na^+ and j) the color changes of ethanol containing 1% phenolphthalein after reaction with N-CNS-1050, k) deconvoluted N 1s spectra of N-CNS-1050 at the stage of the pristine and discharge to 0.2, 0.1, and 0.01 V states.

slope from OCV to 0.01 V. This may be attributed to the highly amorphous and low content of graphitic carbon in HC, which is further confirmed by the negligible shift of (002) peak according to the ex situ XRD pattern (Figure 6d). Therefore, HC anode mainly relies on the adsorption mechanism for sodium ion storage.

By contrast, the intensity and position of *D*-band and *G*-band for N-CNS-1050 anode are strongly affected during the discharge/charging process, as shown in Figure 6e,f. During the discharge process, the intensity of *D*-band is decreased from the open circuit potential (OCV) to 0.1 V, which is attributed to the adsorption of sodium ions on defective sites and the edges of carbon layers, thus limiting the breathing vibration of the sp^2 atoms in the carbon rings. When the voltage reaches 0.01 V in the discharge process, the slight enhancement of *D*-band peak is attributed to the disorder and inhomogeneity of carbon structure caused by the insertion of sodium ion in carbon layers. Meanwhile, the intensity of *G*-band gradually decreases with the drop of discharge potential and almost disappears at the potential of 0.01 V, accompanied by the apparent red-shifted. Notably, when the discharge potential reaches 0.1 V, a new peak located at 1460 cm^{-1} is obviously observed as shown in Figure 6g, which can be ascribed to the insertion of sodium ions into the graphitized carbon layers and is corresponding to the plateau region of the discharge curve. In conclusion, when it enters low potential region (<0.1 V), the *D*-band is slightly enhanced and the *G*-band is rapidly weakened and shifts, indicating the transformation into disordered microstructure

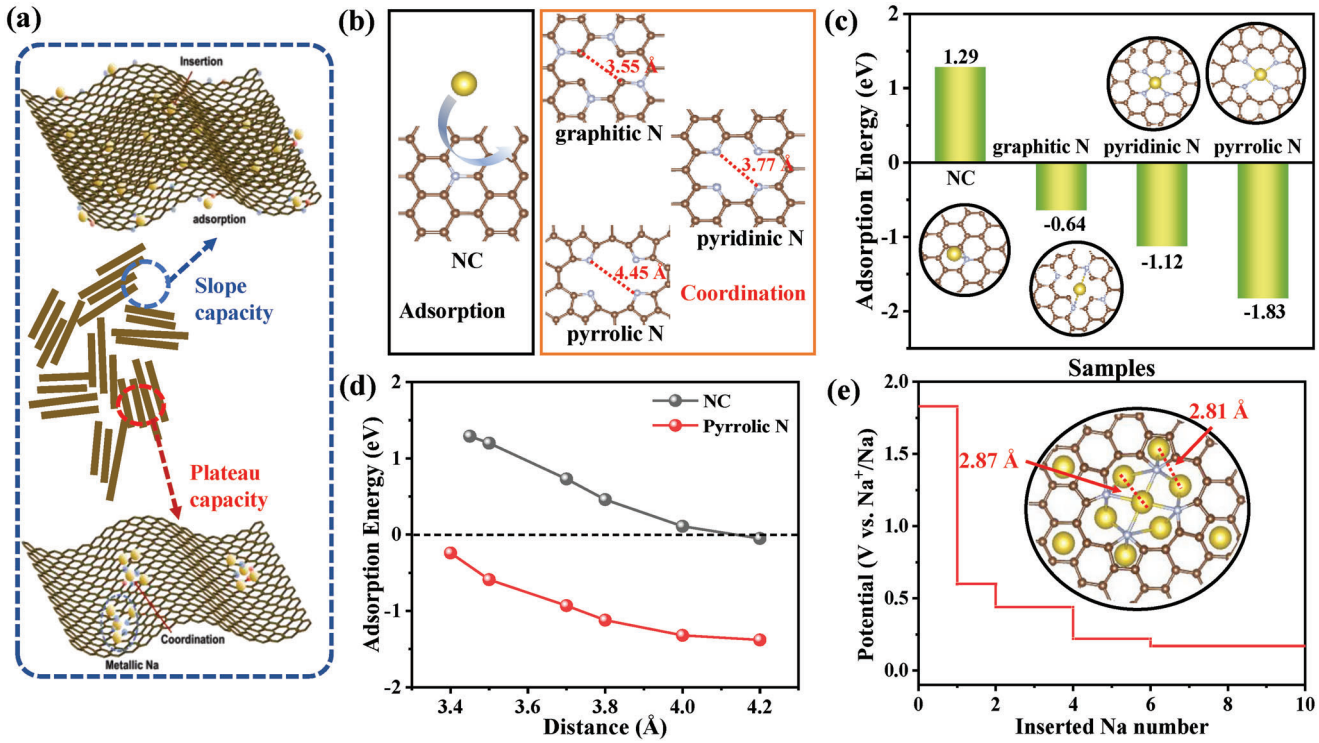

Figure 7. a) Schematic diagram of the source of sodium storage capacities, b) schematic diagram of nitrogen defect structure, c) adsorption energy of Na^+ by different defect structures, d) relationship between interlayer spacing of carbon material and sodium storage adsorption energy, e) sodium storage potential diagram and structure of pyrrolic N.

and is indicative of the filling of sodium into the nanopores. Meanwhile, the relative symmetry of Raman curves during the discharge/charge process indicates good reversibility of the material.

This result is further verified by ex situ XRD, XPS, and ICP analysis. In Figure 6h, the position of (002) peak shifts slightly towards lower angle upon discharge to 0.01 V, indicating an increase in the interlayer spacing, which could validate the insertion of sodium ion into carbon layers. Then, it recovers to the pristine position upon charge to 2.5 V, indicating the good reversibility for sodium ion insertion/extraction. Figure 6i exhibits the ex situ XPS spectra of sodium for N-CNS-1050 at various discharge states. A small wide peak is observed in the Na 1s spectrum of the pristine electrode, in which the sodium ions are provided by the sodium alginate binder. When the discharge potential decreases from 0.2 to 0.01 V, the intensity of Na 1s peak increases gradually and moves towards lower binding energy which gradually approaches the peak position of metal Na, implying the formation of quasi-metallic sodium.

This opinion is further proved by the specific reaction of sodiated N-CNS-1050 anode with protonic ethanol solvent. The concentration of sodium ions is determined by ICP measurements. In Figure 6j, it is observed that the concentration of sodium ion gradually increases and the color of solution containing phenolphthalein indicator gradually deepens, indicating that sodiated electrode reacts with ethanol more and more vigorously, meanwhile more quasi-metallic sodium stored in the electrode is formed with the decrease of discharge potential. In addition, the changes in the intensity and position of the N1s peak in Figure 6k during the discharge process indicate occurrence of the interaction between sodium ions and nitrogen. When the potential is decreased from the pristine state to 0.2 V, the decreased graphitic nitrogen intensity and increased pyrrolic nitrogen intensity, as well as unchanged peak position have been clearly observed, which is likely due to the changed electron cloud density of the conjugated system by the introduction of sodium ions. When the potential drops to 0.01 V, it can be clearly seen that the intensities of pyrrolic N and pyridinic N decrease and their peak positions move towards lower binding energy, indicating that these two types of N configurations can provide active sites for sodium storage in the low potential plateau region and stabilize sodium in the electrode. Based on the above analysis, it is concluded that the sodium ion storage of N-CNS-1050 anode is depended on the adsorption/insertion mechanism coordinating quasi-metallic Na.

The density functional theory (DFT) calculations were carried out to further investigate the storage mechanism of sodium ions. **Figure 7**a is a schematic diagram to explain the capacity source. It is known that the traditional N-doped carbon (NC) mainly relies on the adsorption to store sodium ions.[65] By contrast, the carbon material in this work contains different types of nitrogen defects, which is beneficial to capture the sodium ions through the coordination effect. Here, we simplify the common metal-nitrogen fourfold coordination ($M\text{-}N_4$) model and the single atom structure is available in Figure 7b. It is obvious that different coordination defect sizes expose due to the corresponding nitrogen structures. In other words, the pore sizes of graphitic N, pyridinic N and pyrrolic N are 3.55, 3.77, and 4.45 Å, respectively.

Figure 7c shows the adsorption energies of various defective structures for sodium. It is found that the adsorption energy of NC is +1.29 eV, so the intercalation of sodium could not be carried out, while the coordination structure could easily capture sodium ions. By comparison, it is found that the adsorption energy is positively correlated with the coordination pore size, and the pyrrolic N structure has the best adsorption energy of −1.83 eV. Moreover, Figure 7d depicts the sodium storage capacity of carbon material layer with various spacing. It is found that sodium storage is easier with the increase of layer spacing. Therefore, the sample N-CNS-1050 obtained at 1050 °C could deliver excellent sodium storage performance owing to the large interlayer spacing of 3.88 Å. Figure 7e shows the calculated theoretical sodium storage potential of pyrrolic N. It is found that the low potential platform of 0.15 V delivers high sodium storage capacity, which is consistent with the experimental results. The mechanism of sodium storage may be attributed the formation of metallic sodium cluster structure by nitrogen defect storage, in which the Na−Na bond length is 2.8 Å. The generation of sodium cluster is proved already and the mechanism is reasonable and feasible. Therefore, the sample N-CNS has unique nitrogen defect to enhance the sodium storage capacity.

3. Conclusions

In this manuscript, we have constructed N-doped carbon nanosheets by using CMC-Na as precursor with the assistance of g-C_3N_4. The micromorphology of N-CNS with abundant defects and suitable interlayer spacing are achieved by doping and optimizing the nitrogen radicals formed through the conversion of nitrile intermediates. Therefore, the N-CNS anode delivers high specific capacity of 304.7 mAh g^{-1} at 0.05 A g^{-1} and superior rate capability of 192.8 mAh g^{-1} at 5.0 A g^{-1}, as well as ultra-long cycle life of more than 2000 cycles. The relationship between the microstructure and electrochemical performance of N-CNS anode is illustrated by kinetic analysis, in situ Raman, ex situ XRD, and XPS analysis to deeply understand the sodium storage mechanism. We confirm the mechanism of interlayer sodium ions insertion coordinated quasi-metallic storage in the low potential plateau region. From the perspective of atomic structure, DFT calculations further demonstrate that the interlayer spacing and nitrogen defects play the dominant role in sodium storage mechanism. This work not only provides an in-depth understanding of sodium ion storage, but also provides an effective strategy for rational design of carbon-based anode materials structure.

4. Experimental Section

Preparation of Precursor CMC-Na@g-C_3N_4: 0.5 g of CMC-Na (Aldrich, viscosity: 2000 ± 20 MPa·s) was dissolved in deionized water under strong stirring. Thereafter, 0.5 g of g-C_3N_4 was dispersed in the above solution and stirred vigorously for 2 h to obtain homogeneous suspension. The preparation of g-C_3N_4 was referred to the method in the previous work.[66] The precursor of CMC-Na@g-C_3N_4 can be obtained by freeze-drying for 48 h in the vacuum freeze-dryer.

Synthesis of N-CNS: The precursor of CMC-Na@g-C_3N_4 was placed in a tube furnace and annealed at different temperatures (T = 900, 1050, 1200 °C) for 2 h at the heating rate of 2 °C min^{-1} under the flow of Ar. The as-obtained product was subsequently immersed in diluted HCl solution to remove insoluble substances, then flushed with deionized water for several times, and dried in a vacuum oven at 80 °C for 12 h. After being cleaned and dried, the final sample was obtained and named N-CNS. In addition, a control sample labeled as HC was prepared using the same experimental conditions at the annealing temperature of 1050 °C, but without the addition of g-C_3N_4.

Material Characterization: The crystal structures of as-samples were characterized by XRD (Rigaku Smartlab, Japan) with Cu Kα radiation sources (λ = 1.5418 Å). The FT-IR spectra were performed by using an infrared spectrometer (Nicolet iS10, Thermo Fisher Scientific, the United States of America) equipped with attenuated total reflection. The Raman spectra were recorded by Raman spectrometer (Renishaw inVia, United Kingdom). XPS was conducted on an ESCALAB 250 xi photoelectron spectrometer (Thermo Fisher Scientific, the United States of America) using Al Kα monochromatized radiation. TGA was carried out on a thermal analyser (TGA/DSC 3+, Mettler, Switzerland) at a heating rate of 10 °C min^{-1} in Ar atmosphere. The evolved gases during the sintered progress were determined by synchro-thermogravimetric analyser (STA 449 F5 Jupiter, Netzsch, Germany) coupled to a mass spectrometer (QMS 403 D, Netzsch, Germany). The Branauer–Emmett–Teller (BET) specific surface area and pore size distribution were obtained by using adsorption/desorption analyzer (Micrometrics ASAP 2020, Micromeritics, the United States of America) at 77 K. The optical images were obtained by using the microscope (YueScope YM710R, China). The morphology, structure and element distributions of samples were monitored by SEM (Tescan Mira3, Czech Republic), HRTEM (FEI Tecnai G2 F30, the United States of America) and EDS (Oxford X Max20, Tescan, Czech Republic), respectively. In situ Raman spectra were tested on a Raman spectrometer (WITec alpha300 R, Germany). The concentration of sodium ions in the reaction solution was measured by ICP-OES (Aglient 7800, the United States of America). Ex situ XRD, XPS measurements, the coin cells were disassembled in glove box after reaching the desired voltage and the electrodes were washed by dimethyl carbonate (DMC) and samples were sealed in a foil bottle with Ar filling.

Electrochemical Measurement: The anodes for SIBs were prepared by mixing active material N-CNS, conductive agent carbon black and binder sodium alginate at the weight ratio of 8:1:1 in deionized water under vigorous stirring for 6 h to obtain homogeneous slurry. Then, it was coated on a copper foil collector. Subsequently, it was placed in a vacuum oven at 80 °C for 12 h. The loading mass of active material on working electrode was 1.5 mg cm^{-2}, and the thickness of electrode was about 50 µm. CR2032-type coin cells were assembled in an argon-filled glove box by using glass fiber (Whatman GF/D) as the separator, metallic sodium sheet as the counter electrode, and 1.0 mol L^{-1} $NaPF_6$ dissolved in dimethyl ether (DME) as electrolyte. The assembled batteries were tested for galvanostatic discharge/charge using the Land battery test system (CT-2001A, Wuhan, China) with the range of voltage 0.0–2.5 V (vs. Na^+/Na). CV tests were conducted on CHI660E electrochemical workstation. EIS was also measured on the same electrochemical workstation between the frequency range of 10^{-2}–10^5 Hz with an amplitude of 5 mV.

Computational Method: All the DFT computations were conducted by using Vienna Ab initio Simulation Package (VASP5.4.4) via projector-augmented wave pseudopotentials. The generalized gradient approximation (GGA) with the PredewBurke-Ernzerh (PBE) of function was used for the exchange-correlation interaction. The total energy change during the structure optimization processes was ultimately converged to 5×10^{-6} eV. In addition, the forces per atom were reduced to 0.01 eV $Å^{-1}$. The k-point mesh of the Brillouin zone was set at 2 × 2 × 1 for geometry optimization. A cutoff energy of 450 eV was adopted during the computations. The formation energy of the product was calculated by the Equation (6).

$$\Delta G\,(\mathrm{Na-HC}) = G\,(\mathrm{Na-HC}) - G\,(\mathrm{HC}) - G\,(\mathrm{Na}) \quad (6)$$

where the G(Na−HC) was the total Gibbs energies of the absorbate of HC and Na, G(HC) and G(Na) were the Gibbs energies of HC structure and Na, respectively.

In addition, the voltage was calculated as the Equation (7).

$$E = -\Delta G\,(n\mathrm{Na} - \mathrm{HC})\,/nF \quad (7)$$

where the $\Delta G(n\mathrm{Na}-\mathrm{HC})$, n and F were the formation energy of the adsorbate, electron number and Faraday constant (96 485 C mol^{-1}).

Supporting Information

Supporting Information is available from the Wiley Online Library or from the author.

Acknowledgements

This work was supported by the National Natural Science Foundation of China (No. 51972104, 51672079, U21A2081, 22075074), Outstanding Young Scientists Research Funds from Hunan Province (2020JJ2004), and Science and Technology Plan Projects of Hunan Province (No. 2017TP1009).

Conflict Of Interest

The authors declare no conflict of interest.

Data Availability Statement

Research data are not shared.

Keywords

density functional theory calculations, hard carbon, in situ characterization, sodium storage mechanism, sodium-ion batteries

Received: April 19, 2023
Revised: May 23, 2023
Published online: June 9, 2023

[1] C. Liu, F. Li, L. P. Ma, H. M. Cheng, *Adv. Mater.* **2010**, *22*, E28.
[2] J. B. Goodenough, K. S. Park, *J. Am. Chem. Soc.* **2013**, *135*, 1167.
[3] L. L. Tian, X. Y. Wei, Q. C. Zhuang, C. H. Jiang, C. Wu, G. Y. Ma, X. Zhao, Z. M. Zong, S. G. Sun, *Nanoscale* **2014**, *6*, 6075.
[4] Q. Bai, L. Yang, H. Chen, Y. Mo, *Adv. Energy Mater.* **2018**, *8*, 1702998.
[5] N. Yabuuchi, K. Kubota, M. Dahbi, S. Komaba, *Chem. Rev.* **2014**, *114*, 11636.
[6] M. D. Slater, D. Kim, E. Lee, C. S. Johnson, *Adv. Funct. Mater.* **2013**, *23*, 947.
[7] Z. L. Xu, J. Park, G. Yoon, H. Kim, K. Kang, *Small Methods* **2018**, *3*, 1800227.
[8] Y. Liu, B. V. Merinov, W. A. Goddard III, *Proc. Natl. Acad. Sci. U. S. A.* **2016**, *113*, 3735.
[9] Y. Wen, K. He, Y. Zhu, F. Han, Y. Xu, I. Matsuda, Y. Ishii, J. Cumings, C. Wang, *Nat. Commun.* **2014**, *5*, 4033.
[10] J. Xu, M. Wang, N. P. Wickramaratne, M. Jaroniec, S. Dou, L. Dai, *Adv. Mater.* **2015**, *27*, 2042.
[11] Y. Li, L. Mu, Y. S. Hu, H. Li, L. Chen, X. Huang, *Energy Storage Mater.* **2016**, *2*, 139.
[12] Y. Liu, Y. Xu, Y. Zhu, J. N. Culver, C. A. Lundgren, K. Xu, C. Wang, *ACS Nano* **2013**, *7*, 3627.
[13] Y. Yuan, S. Jan, Z. Wang, X. Jin, *J. Mater. Chem. A* **2018**, *6*, 5555.
[14] B. Zhang, J. Huang, J. K. Kim, *Adv. Funct. Mater.* **2015**, *25*, 5222.
[15] H. Xiong, M. D. Slater, M. Balasubramanian, C. S. Johnson, T. Rajh, *J. Phys. Chem. Lett.* **2011**, *2*, 2560.
[16] X. Geng, Y. Jiao, Y. Han, A. Mukhopadhyay, L. Yang, H. Zhu, *Adv. Funct. Mater.* **2017**, *27*, 1702998.
[17] Z. Liu, A. Daali, G. L. Xu, M. Zhuang, X. Zuo, C. J. Sun, Y. Liu, Y. Cai, M. D. Hossain, H. Liu, K. Amine, Z. Luo, *Nano Lett.* **2020**, *20*, 3844.
[18] X. Zhong, Y. Li, L. Zhang, J. Tang, X. Li, C. Liu, M. Shao, Z. Lu, H. Pan, B. Xu, *ACS Appl. Mater. Interfaces* **2019**, *11*, 2970.
[19] C. Ding, L. Huang, J. Lan, Y. Yu, W. H. Zhong, X. Yang, *Small* **2020**, *16*, 1906883.
[20] K. Huo, W. An, J. Fu, B. Gao, L. Wang, X. Peng, G. J. Cheng, P. K. Chu, *J. Power Sources* **2016**, *324*, 233.
[21] Y. Li, Y. S. Hu, M. M. Titirici, L. Chen, X. Huang, *Adv. Energy Mater.* **2016**, *6*, 1600659.
[22] Z. Wang, K. Dong, D. Wang, S. Luo, Y. Liu, Q. Wang, Y. Zhang, A. Hao, C. Shi, N. Zhao, *J. Mater. Chem. A* **2019**, *7*, 14309.
[23] D. Wang, K. H. Tian, J. Wang, Z. Y. Wang, S. H. Luo, Y. G. Liu, Q. Wang, Y. H. Zhang, A. M. Hao, T. F. Yi, *Rare Met.* **2021**, *40*, 2464.
[24] Y. Tang, X. Wang, J. Chen, D. Wang, Z. Mao, *Chem. Eng. J.* **2022**, *427*, 131951.
[25] Y. Huang, K. Tang, F. Yuan, W. Zhang, B. Li, F. Seidi, H. Xiao, D. Sun, *Carbon* **2020**, *168*, 12.
[26] Z. Li, C. Bommier, Z. S. Chong, Z. Jian, T. W. Surta, X. Wang, Z. Xing, J. C. Neuefeind, W. F. Stickle, M. Dolgos, P. A. Greaney, X. Ji, *Adv. Energy Mater.* **2017**, *7*, 1602894.
[27] L. Qie, W. Chen, X. Xiong, C. Hu, F. Zou, P. Hu, Y. Huang, *Adv. Sci.* **2015**, *2*, 1500195.
[28] M. Hao, N. Xiao, Y. Wang, H. Li, Y. Zhou, C. Liu, J. Qiu, *Fuel Process. Technol.* **2018**, *177*, 328.
[29] J. Liu, Y. Zhang, L. Zhang, F. Xie, A. Vasileff, S. Z. Qiao, *Adv. Mater.* **2019**, *31*, 1901261.
[30] J. Yang, X. Zhou, D. Wu, X. Zhao, Z. Zhou, *Adv. Mater.* **2017**, *29*, 1604108.
[31] P. Lu, Y. Sun, H. Xiang, X. Liang, Y. Yu, *Adv. Energy Mater.* **2018**, *8*, 1702434.
[32] D. Xu, C. Chen, J. Xie, B. Zhang, L. Miao, J. Cai, Y. Huang, L. Zhang, *Adv. Energy Mater.* **2016**, *6*, 1501929.
[33] H. Liu, M. Jia, B. Cao, R. Chen, X. Lv, R. Tang, F. Wu, B. Xu, *J. Power Sources* **2016**, *319*, 195.
[34] W. Hong, Y. Zhang, L. Yang, Y. Tian, P. Ge, J. Hu, W. Wei, G. Zou, H. Hou, X. Ji, *Nano Energy* **2019**, *65*, 104038.
[35] D. A. Stevens, J. R. Dahn, *J. Electrochem. Soc.* **2000**, *147*, 1271.
[36] Y. Cao, L. Xiao, M. L. Sushko, W. Wang, B. Schwenzer, J. Xiao, Z. Nie, L. V. Saraf, Z. Yang, J. Liu, *Nano Lett.* **2012**, *12*, 3783.
[37] X. Chen, J. Tian, P. Li, Y. Fang, Y. Fang, X. Liang, J. Feng, J. Dong, X. Ai, H. Yang, Y. Cao, *Adv. Energy Mater.* **2022**, *12*, 2200886.
[38] S. Huang, Z. Li, B. Wang, J. Zhang, Z. Peng, R. Qi, J. Wang, Y. Zhao, *Adv. Funct. Mater.* **2018**, *28*, 1706294.
[39] S. Qiu, L. Xiao, M. L. Sushko, K. S. Han, Y. Shao, M. Yan, X. Liang, L. Mai, J. Feng, Y. Cao, X. Ai, H. Yang, J. Liu, *Adv. Energy Mater.* **2017**, *7*, 1700403.
[40] P. Bai, Y. He, X. Zou, X. Zhao, P. Xiong, Y. Xu, *Adv. Energy Mater.* **2018**, *8*, 1703217.
[41] H. Yamamoto, S. Muratsubaki, K. Kubota, M. Fukunishi, H. Watanabe, J. Kim, S. Komaba, *J. Mater. Chem. A* **2018**, *6*, 16844.
[42] Y. Zhang, Y. Meng, Y. Wang, L. Chen, Y. Guo, D. Xiao, *ChemElectroChem* **2017**, *4*, 500.
[43] T. Zhang, J. Chen, B. Yang, H. Li, S. Lei, X. Ding, *RSC Adv.* **2017**, *7*, 50336.
[44] X. Qi, K. Huang, X. Wu, W. Zhao, H. Wang, Q. Zhuang, Z. Ju, *Carbon* **2018**, *131*, 79.

[45] Y. Tang, X. Wang, J. Chen, X. Wang, D. Wang, Z. Mao, *Carbon* **2021**, *174*, 98.
[46] J. Li, Y. Zhang, X. Zhang, J. Han, Y. Wang, L. Gu, Z. Zhang, X. Wang, J. Jian, P. Xu, B. Song, *ACS Appl. Mater. Interfaces* **2015**, *7*, 19626.
[47] L. Xiao, Y. Cao, W. A. Henderson, M. L. Sushko, Y. Shao, J. Xiao, W. Wang, M. H. Engelhard, Z. Nie, J. Liu, *Nano Energy* **2016**, *19*, 279.
[48] H. Zhang, Y. Yang, D. Ren, L. Wang, X. He, *Energy Storage Mater.* **2021**, *36*, 147.
[49] N. Sun, Z. Guan, Y. Liu, Y. Cao, Q. Zhu, H. Liu, Z. Wang, P. Zhang, B. Xu, *Adv. Energy Mater.* **2019**, *9*, 1901351.
[50] Y. Reynier, R. Yazami, B. Fultz, I. Barsukov, *J. Power Sources* **2007**, *165*, 552.
[51] S. Jia, J. Wei, X. Meng, Z. Shao, *Electrochim. Acta* **2020**, *331*, 135338.
[52] H. Yu, L. Shang, T. Bian, R. Shi, G. I. Waterhouse, Y. Zhao, C. Zhou, L. Z. Wu, C. H. Tung, T. Zhang, *Adv. Mater.* **2016**, *28*, 5080.
[53] E. Raymundo-Piñero, M. Cadek, F. Béguin, *Adv. Funct. Mater.* **2009**, *19*, 1032.
[54] J. Chen, Z. Mao, L. Zhang, D. Wang, R. Xu, L. Bie, B. D. Fahlman, *ACS Nano* **2017**, *11*, 12650.
[55] Y. Tang, X. Wang, J. Chen, X. Wang, D. Wang, Z. Mao, *Carbon* **2020**, *168*, 458.
[56] M. Wang, Z. Yang, W. Li, L. Gu, Y. Yu, *Small* **2016**, *12*, 2559.
[57] X. Hu, X. Sun, S. J. Yoo, B. Evanko, F. Fan, S. Cai, C. Zheng, W. Hu, G. D. Stucky, *Nano Energy* **2019**, *56*, 828.
[58] B. Cao, H. Liu, B. Xu, Y. Lei, X. Chen, H. Song, *J. Mater. Chem. A* **2016**, *4*, 6472.
[59] R. Guo, C. Lv, W. Xu, J. Sun, Y. Zhu, X. Yang, J. Li, J. Sun, L. Zhang, D. Yang, *Adv. Energy Mater.* **2020**, *10*, 1903652.
[60] K. Hong, L. Qie, R. Zeng, Z. Yi, W. Zhang, D. Wang, W. Yin, C. Wu, Q. Fan, W. Zhang, Y. Huang, *J. Mater. Chem. A* **2014**, *2*, 12733.
[61] K. Tang, L. Fu, R. J. White, L. Yu, M. M. Titirici, M. Antonietti, J. Maier, *Adv. Energy Mater.* **2012**, *2*, 873.
[62] L. Yang, M. Hu, H. Zhang, W. Yang, R. Lv, *J. Colloid Interface Sci.* **2020**, *566*, 257.
[63] F. Sun, H. Wang, Z. Qu, K. Wang, L. Wang, J. Gao, J. Gao, S. Liu, Y. Lu, *Adv. Energy Mater.* **2021**, *11*, 2002981.
[64] Q. Gan, N. Qin, S. Gu, Z. Wang, Z. Li, K. Liao, K. Zhang, L. Lu, Z. Xu, Z. Lu, *Small Methods* **2021**, *5*, 2100580.
[65] R. R. Gaddam, A. H. Farokh Niaei, M. Hankel, D. J. Searles, N. A. Kumar, X. S. Zhao, *J. Mater. Chem. A* **2017**, *5*, 22186.
[66] Y. Zhao, Z. Hu, C. Fan, Z. Liu, R. Zhang, S. Han, J. Liu, J. Liu, *Chem. Eng. J.* **2022**, *446*, 137427.